The Astrophysical Journal Supplement Series, 216:23 (13pp), 2015 February doi:10.1088/0067-0049/216/2/23

EXO-ZODI MODELING FOR THE LARGE BINOCULAR TELESCOPE INTERFEROMETER

Grant M. Kennedy[1], Mark C. Wyatt[1], Vanessa Bailey[2], Geoffrey Bryden[3], William C. Danchi[4], Denis Defrère[2], Chris Haniff[5], Philip M. Hinz[2], Jérémy Lebreton[6,7], Bertrand Mennesson[3], Rafael Millan-Gabet[7], Farisa Morales[3], Olja Panić[1], George H. Rieke[2], Aki Roberge[4], Eugene Serabyn[3], Andrew Shannon[1], Andrew J. Skemer[2], Karl R. Stapelfeldt[4], Katherine Y. L. Su[2], and Alycia J. Weinberger[8]
[1] Institute of Astronomy, University of Cambridge, Madingley Road, Cambridge CB3 0HA, UK
[2] Steward Observatory, University of Arizona, 933 North Cherry Avenue, Tucson, AZ 85721, USA
[3] Jet Propulsion Laboratory, California Institute of Technology, 4800 Oak Grove Drive, Pasadena, CA 91109, USA
[4] NASA Goddard Space Flight Center, Exoplanets and Stellar Astrophysics, Code 667, Greenbelt, MD 20771, USA
[5] Cavendish Laboratory, University of Cambridge, JJ Thomson Avenue, Cambridge CB3 0HE, UK
[6] Infrared Processing and Analysis Center, MS 100-22, California Institute of Technology, 770 South Wilson Avenue, Pasadena, CA 91125, USA
[7] NASA Exoplanet Science Institute, California Institute of Technology, 770 South Wilson Avenue, Pasadena, CA 91125, USA
[8] Department of Terrestrial Magnetism, Carnegie Institution of Washington, 5241 Broad Branch Road NW, Washington, DC 20015, USA
Received 2014 October 1; accepted 2014 November 14; published 2015 January 27

ABSTRACT

Habitable zone dust levels are a key unknown that must be understood to ensure the success of future space missions to image Earth analogs around nearby stars. Current detection limits are several orders of magnitude above the level of the solar system's zodiacal cloud, so characterization of the brightness distribution of exo-zodi down to much fainter levels is needed. To this end, the Large Binocular Telescope Interferometer (LBTI) will detect thermal emission from habitable zone exo-zodi a few times brighter than solar system levels. Here we present a modeling framework for interpreting LBTI observations, which yields dust levels from detections and upper limits that are then converted into predictions and upper limits for the scattered light surface brightness. We apply this model to the HOSTS survey sample of nearby stars; assuming a null depth uncertainty of 10^{-4} the LBTI will be sensitive to dust a few times above the solar system level around Sun-like stars, and to even lower dust levels for more massive stars.

Key words: circumstellar matter – instrumentation: interferometers – zodiacal dust

1. INTRODUCTION

One of the major long-term goals of astronomy is to place the solar system within a greater context, finding for example whether habitable planets like the Earth are typical, and whether these Earth analogs have conditions suitable for alien life. Such goals are ambitious and many obstacles must be overcome for them to come to fruition.

For the particular case of directly imaging Earth-like planets around other stars, a major unknown is the level of photon noise from the dust that resides in the target system itself, specifically dust located in the "habitable zone" (HZ; e.g., Kasting et al. 1993). Such dust populations are generically referred to as "exo-zodi" by analogy with the solar system's zodiacal cloud, though they may have different origins. To be clear, we consider the dust populations seen around 10%–25% of nearby stars with near-infrared (IR) interferometry to be a largely unrelated phenomenon, based on their small grain size and hot temperatures (e.g., Defrère et al. 2011; Lebreton et al. 2013), and lack of correlation with both mid-IR detections of HZ dust (Mennesson et al. 2014) and far-IR detections of cool dust (Absil et al. 2013; Ertel et al. 2014).

If HZ dust levels an order of magnitude or so greater than the solar system level are typical, this noise source could seriously hinder an Earth analog-imaging and characterization mission (which we will refer to as "Earth-imaging" for brevity, e.g., Absil et al. 2010; Roberge et al. 2012; Stark et al. 2014; Brown 2014). Currently, the brightness distribution (which we also call the luminosity function) of exo-zodi is largely unknown. Limits have been set by the Keck Interferometer Nuller (KIN; Serabyn et al. 2012; Millan-Gabet et al. 2011; Mennesson et al. 2014), but the distribution has only been characterized at levels 3–4 orders of magnitude above the solar system by photometric methods (Kennedy & Wyatt 2013).

Enter the Large Binocular Telescope Interferometer (LBTI), a mid-IR instrument specifically designed to characterize exo-zodi at dust levels just a few times greater than the solar system's zodiacal cloud. For a brief description of the instrument see Defrère et al. (2015). By observing of the order of 50 nearby stars at this level of sensitivity (Weinberger et al. 2015), the LBTI will identify specific targets with low dust levels that are suitable for future Earth-imaging, and moreover will characterize the exo-zodi luminosity function with sufficient detail to provide new information on the dust origin and evolution. This latter point is important because the LBTI will observe a limited number of stars and cannot access the entire sky, and population-level information such as correlations with other system properties will be needed to assess the suitability of targets that are not observed with the LBTI.

Of course the results will also be scientifically valuable and interesting, particularly when combined with existing and future observations (e.g., Defrère et al. 2015). Mid and far-IR imaging using telescopes such as *Spitzer, Herschel*, and *James Webb Space Telescope* (*JWST*) will provide important information on the existence, location, and structure of cooler dust belts that lie outside the HZ. Interferometric observations with longer baselines (e.g., VLTI/MATISSE) and/or at different wavelengths (e.g., CHARA/FLUOR, VLTI/PIONIER) will provide information that complements the LBTI to help build a complete picture of the inner regions of individual systems.

The goal of this paper is to outline a modeling framework for interpreting LBTI observations. Such models are needed because LBTI observations yield limited information on the spatial structure of any disk that is detected. It is therefore

important that the model used to interpret the observations is thoroughly characterized so that the constraints placed on its various parameters can be understood in terms of their implications for the disk structure and surface brightness. The primary goal is to use the model to make a useful statement about the level of dust in a system, or the limits on undetected dust, in the habitable zone where Earth-imaging will be attempted in the future.

In what follows, we outline a parameterized dust model that can be used to approximate the solar system's zodiacal dust cloud. We show how this model can be used to derive the distribution of dust levels given an LBTI observation of thermal dust emission. We then determine the corresponding implications for scattered light levels at visible wavelengths. We finally show the expected levels of dust that could be detected by the Hunt for Observable Signatures of Terrestrial Planetary Systems (HOSTS) survey and the corresponding scattered light levels. For a detailed description of the LBTI sample we refer the reader to Weinberger et al. (2015), and for discussion of the instrument and the first scientific results to Defrère et al. (2015).

2. PHYSICAL MODEL

The primary goal of our exo-zodiacal cloud model is to allow easy comparison of the results among survey stars, which span a range of distances and luminosities. In general, we expect that detections will be near the sensitivity limits, and that there will be little information about any warm dust detected (or not detected) other than from LBTI. Therefore, while warm dust may arise from various different processes, for example, in situ Asteroid-belt like evolution, stochastic collisions, delivery of comets from elsewhere, or some combination of all three (e.g., Wyatt et al. 2007; Nesvorný et al. 2010; Jackson & Wyatt 2012; Kennedy & Wyatt 2013), we will have little power to distinguish among them. Some scenarios could result in clumpy non-axisymmetric structures, but there again is little hope of distinguishing these from axisymmetric structures in all but the dustiest systems where LBTI detections will be relatively easy and at high signal-to-noise ratios (S/Ns). Therefore, the models considered here are axisymmetric.

2.1. The Star

For specific stars, the stellar luminosity $L_\star$ (in solar units) is easily derived by fitting stellar atmosphere models to photometry, and the flux density $F_{\nu,\star}$ at any wavelength can be inferred from these models. Given a distance d, the stellar radius can be estimated from the same model, though in some cases it may have been directly observed. In any case, the contribution of the resolved stellar disk to an LBTI observation will generally be negligible. Here we use the stellar fluxes for HOSTS survey stars derived by Weinberger et al. (2015).

2.2. The Disk

LBTI observations are sensitive to the surface brightness distribution $S_{\rm disk}$ in the N' band at 11 μm (the bandpass spans 9.81–12.41 μm). Our model can be considered a means of parameterizing this surface brightness distribution using parameters that have some physical relevance. Unless stated otherwise, in what follows our calculations are made at 11 μm.

The surface brightness profile of the disk, if viewed face-on, is modeled as

$$S_{\rm disk} = 2.35 \times 10^{-11} \Sigma_{\rm m} B_\nu(\lambda, T_{\rm BB}). \quad (1)$$

Here $T_{\rm BB}$ is the temperature of disk material that behaves like a black body

$$T_{\rm BB}(r) = 278.3 L_\star^{0.25} r^{-0.5} {\rm K}, \quad (2)$$

where the distance to the star, r, is in AU. The numerical factor in Equation (1) is a conversion (1 AU^2/1 pc^2) so that the surface brightness is in units of Jy arcsec^{-2}. The parameter $\Sigma_{\rm m}$ is representative of the disk's face-on surface density of cross-sectional area (in AU^2/AU^2), so is analogous to optical depth and is assumed to have a power-law distribution

$$\Sigma_{\rm m}(r) = z\Sigma_{\rm m,0}(r/r_0)^{-\alpha} \quad (3)$$

between radii $r_{\rm in}$ and $r_{\rm out}$ (both in AU). The normalization $\Sigma_{\rm m,0}$ is to be set at some r_0 (in AU) such that the surface density is in units of zodis z (see Section 2.2.3).

For generality we include an inclination I, which is half the total opening angle of the disk, and represents the maximum inclination of the parent bodies (whose nodes would be assumed to be randomized). Here we assume that our disks have negligible opening angles so I is not used, but that I is always sufficiently large that the disk is radially optically thin.

If all of the disk particles behave like black bodies, the parameter $\Sigma_{\rm m}$ can be interpreted as the disk's surface density of cross-sectional area. Its interpretation becomes more complicated for disks with more realistic particle optical properties because the observed dust can be several times hotter than the black body temperature, and not all radiation incident on a particle is absorbed and thermally re-emitted. However, as the surface brightness is typically assumed to exhibit a power-law dependence across the relevant radius range, we have not lost any generality by expressing the disk surface brightness in this way, even if the disk's temperature profile differs from that of a black body. These issues will be discussed in more detail in Sections 2.6 and 2.7.

The final parameters, which specify the direction to the observer relative to the disk, are the disk inclination i and the position angle Ω. The inclination is defined such that $i = 0$ is face-on and the position angle is measured anticlockwise (i.e., east) from north. The range of inclinations is 0 to 90° and the range of position angles 0 to 180°,[9] with these ranges set because we cannot distinguish between the near and far side of a disk. That is, the faint disks considered here are optically thin viewed from any direction, and in thermal emission look the same mirrored in the sky plane or for 180° rotations. The model parameters and their meanings are summarized in Table 1.

2.2.1. `Zodipic`

`Zodipic` is an implementation of the Kelsall et al. (1998) zodiacal cloud model.[10] This parametric model has many parameters, whose values were derived via fitting to *COBE*/DIRBE observations. `Zodipic` produces two-dimensional images of the solar system's zodiacal dust cloud as might be seen by an external observer, and has been used as a reference model for calculating the limits set by KIN observations (Millan-Gabet et al. 2011). Though it is a complex model and can include dust components such as the Earth's resonant ring and trailing blob, only the main smooth axisymmetric component is normally

[9] The symmetry of the LBTI transmission pattern (described in Section 2.3) means that if the disks are not spatially resolved, we in fact only need to consider angles between 0 and 90°. We retain the larger range because we may wish to set Ω based on the position angle of the star or an outer disk component.

[10] Freely available IDL software written by M. Kuchner.

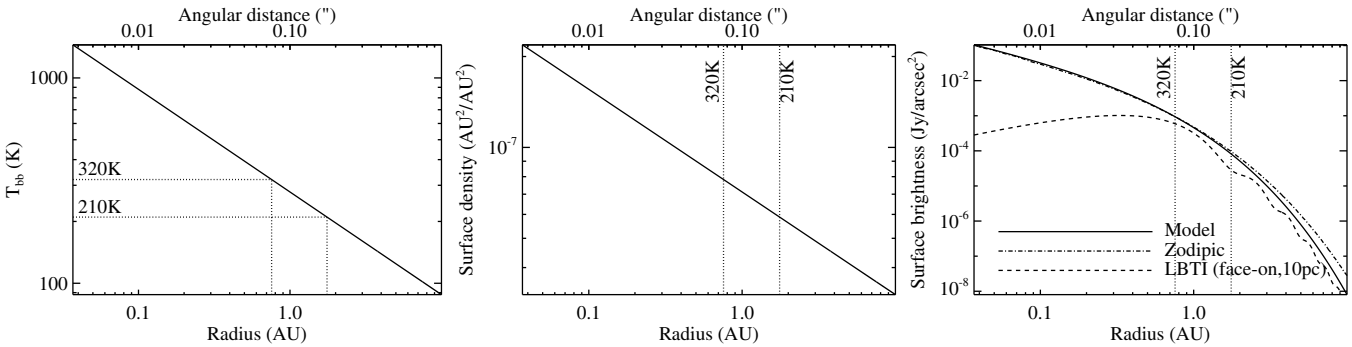

Figure 1. Reference disk model as described in Section 2.2.2, with an approximate habitable zone between 210 and 320 K marked by dotted lines. The left panel shows the model temperature. The middle panel shows the disk surface density of cross sectional area. The right panel shows the disk surface brightness of our reference model (solid line) and an equivalent `Zodipic` model for comparison (dot-dashed line), and the flux that would be transmitted through the LBTI for our reference model disk seen face-on at 10 pc (dashed line).

Table 1
Model Parameters

Symbol	Unit	Parameter	Reference
d	pc	Distance to star+disk system	···
$L_\star$	$L_\odot$	Stellar luminosity	1
$F_\star$	Jy	Stellar flux density at wavelength λ	···
$R_\star$	$R_\odot$	Stellar radius	1
$r_{\rm in}$	AU	Inner disk radius (1500 K)	0.034
$r_{\rm out}$	AU	Outer disk radius (88 K)	10
r_0	AU	Reference radius ($=\sqrt{L_\star/L_\odot}$ AU)	1
$\Sigma_{\rm m,0}$	···	Surface density at r_0 for a $z = 1$ disk	7.12×10^{-8}
z	···	Surface density at r_0 in zodis	1
α	···	Index for $\Sigma_{\rm m}$	0.34
I	°	Disk half-opening angle	small
i	°	Disk inclination relative to face-on	···
Ω	°	Disk position angle E of N on the sky	···

Notes. Model parameters are separated into those related to the star, disk, and observation. The rightmost column gives parameters for the reference disk model.

used. Because this main component is simply a radial power law, with an approximately Gaussian vertical density distribution, it is possible to reproduce the `Zodipic` surface brightness using our parameterized model.

The vertical dust distribution is the main difference between the Kelsall et al. (1998) model and ours. The Kelsall et al. (1998) model assumes that the radial and vertical components of the cloud are separable

$$n = n_0 r^{-p} \exp\left(-\beta g^\gamma\right), \quad (4)$$

where

$$g = \begin{cases} \xi^2/2\mu & \xi < \mu \\ \xi - \mu/2 & \xi \geqslant \mu \end{cases}, \quad (5)$$

$\xi = |Z/r|$, and Z is the height above the disk midplane in AU. The best-fit values for the *COBE* data were $n_0 = 1.13 \times 10^{-7}$, $p = 1.34$, $\beta = 4.14$, $\gamma = 0.942$, and $\mu = 0.189$. The units of the normalization are AU^2/AU^3 (i.e., a volume density of surface area), and the integrated length of the vertical term is not constant with radius, so their exponent p is not the same as our exponent α. Numerically integrating Equation (5) over $-\infty < \xi < \infty$ yields 0.63, so the surface density at 1 AU is 7.12×10^{-8} (AU^2/AU^2). Assuming for mathematical simplicity that $\gamma = 1$, the integral of the exponential term in Equation (4) is $\propto r$ for both cases of g, and hence $\alpha \approx p - 1$ and $\alpha \approx 0.34$. Therefore, the `Zodipic` model can be reasonably expressed in terms of our model with $r_0 = 1$ AU $\Sigma_{\rm m,0} = 7.12 \times 10^{-8}$, and $\alpha = 0.34$.

There remain a few small differences in the surface brightness of our model relative to `Zodipic`, as shown in the right panel of Figure 1. The main difference is that the `Zodipic` model is slightly brighter at larger radii because the radial temperature profile is flatter. Setting the `Zodipic` temperature profile to equal our black body prescription leads to nearly indistinguishable face-on surface brightness profiles. Some minor differences arise because the Kelsall et al. (1998) model defines radius as $r = \sqrt{x^2 + y^2 + z^2}$, whereas our narrow opening angle means that our model is effectively cylindrical.

2.2.2. Reference Model

Here we introduce a reference disk model, the parameters of which are summarized in Table 1 and based on the Kelsall et al. (1998) solar system model described above. The model extends from 0.034–10 AU with a power-law index $\alpha = 0.34$, and is scaled to $\Sigma_{\rm m,0} = 7.12 \times 10^{-8}$ at $r_0 = 1$ AU (the location where $T_{\rm BB} = 278.3$ K). The inner edge is set by a black body temperature of 1500 K, approximately the sublimation temperature of silicates, though we show in Section 2.6 that this choice is irrelevant for our model as long as the inner disk edge is inside the IWA of 40 mas. The outer edge of 10 AU is chosen to be sufficiently large that it does not affect the model at the LBTI wavelength of 11 μm. As noted above we treat the disk as two dimensional so the opening angle is small. Our reference model is based on the solar system so the star is Sun-like, but as described in Section 2.2.3 the reference parameters are later varied to model disks around different stars.

Figure 1 shows the distribution of temperature, surface density and surface brightness at 11 μm in this reference model, where we have assumed a distance of 10 pc. Survey targets are chosen so that the LBTI is sensitive to dust in their habitable zone (Weinberger et al. 2015), so the dotted lines show the range of radii implied by a temperature range of 210–320 K, a rough indication of the habitable zone location for the Sun (e.g., Kopparapu et al. 2013). The right panel shows that the surface brightness of our model closely matches `Zodipic`, and as noted above this difference only arises due to different assumptions about the radial temperature profile. Therefore, for the same assumptions and aside from the differences in scale height, our model yields the same results as `Zodipic` for a Sun-like star.

2.2.3. Normalization (What is a Zodi?)

The disk normalization (i.e., brightness) is set by the parameter $\Sigma_{m,0}$, which is the disk surface density at r_0. The goal here is to set what $\Sigma_{m,0}$ and r_0 are so that they scale sensibly with stellar spectral type, and so that our disk model is somehow sensibly related to zodi units, and therefore the solar system dust level. These parameters, along with r_{in}, r_{out}, α, and I define our reference disk model. In making this definition, it is important to remember the ultimate goal of the LBTI, which is to constrain the level of dust in the habitable zone around nearby stars. That is, disk surface brightness is the most important measure of the impact of exo-zodi on future Earth-imaging missions.

A desirable definition might be one of "constant hindrance" for an Earth-imaging mission, where $\Sigma_{m,0}$ is set such that a $z = 1$ disk impacts all observations in search of exo-Earths at the same level. However, for this imaging any exo-Earths will be unresolved, whereas the exo-zodi that accompany them will be resolved, so the same physical disk has the same surface brightness regardless of distance, but the brightness of the unresolved planet decreases with distance. Therefore, any zodi definition that attempts to provide constant hindrance will be distance dependent, which is an undesirable property since it is unrelated to the physical disk structure.

To set $\Sigma_{m,0}$ therefore requires a choice between using either the total disk brightness, or the surface brightness at r_0. Both approaches have their merits. For example, using the total disk brightness allows comparison with photometric observations and therefore easy construction of the warm dust luminosity function (e.g., Kennedy & Wyatt 2013). However, as we show below in Figure 4, LBTI observations are not necessarily sensitive to total disk brightness (e.g., when a significant fraction of the disk emission lies inside the first transmission peak).

We therefore prefer a zodi definition linked to the disk surface density in the habitable zone. For the spectral type scaling, it then makes sense for r_0 to scale with $\sqrt{L_\star}$, so that the surface brightness expressed by $\Sigma_{m,0}$ corresponds to the radial distance where the equilibrium temperature is the same as at Earth (i.e., an "Earth-equivalent" distance), therefore $r_0 = \sqrt{L_\star/L_\odot}$ AU. Scaling r_{in} and r_{out} by $\sqrt{L_\star/L_\odot}$ is also appropriate, since this results in a common temperature at the inner and outer edges of the disk, and maintains the disk inner edge at the sublimation radius. The disk edges are of relatively little importance here because as we show below the LBTI is relatively insensitive to their location.

With this definition, $\Sigma_{m,0}$ is fixed at the surface density of the solar system's zodiacal cloud at 1 AU, but the location where this surface density applies depends on the stellar luminosity. This definition is different to `Zodipic`, which fixes r_0 at 1 AU for all stars and fixes r_{in} at the sublimation radius. Because the dust temperature at r_0 is the same for all spectral types, the thermal surface brightness at r_0 (i.e., in the habitable zone) for a 1 zodi disk is also the same. Because it is based on surface brightness, this zodi definition is well suited for use as an important metric for future Earth-imaging missions.

An LBTI observation is not necessarily sensitive to the radial extent of a disk, so the derived zodi level depends on what is assumed for r_{in} and r_{out}, particularly if the disk is relatively narrow. For example, below we consider a "worst case" scenario where the dust emission only originates in the habitable zone, in which case the derived dust surface density (and hence z) is higher for a given null depth. To avoid confusion we recommend that zodi levels primarily use our reference model to allow consistent comparisons.

2.3. Transmission through the LBTI Fringe Pattern

The original concept for nulling interferometry was put forward by Bracewell (1978), and for a reasonably non-technical description of the instrument we refer the reader to Defrère et al. (2015). Basically speaking, the LBTI combines the beams from the two LBT mirrors, with one beam having a half-wavelength phase shift. Light in the viewing direction, and along lines perpendicular to the mirror baseline vector, is therefore suppressed. Light from off axis sources at odd multiples of the angular distance $\lambda/(2B)$ is transmitted (B is the baseline length). Similarly, light from sources at even multiples of this angular distance is suppressed. The transmission (or "fringe") pattern is therefore a $\sin^2$ function parallel to the baseline vector, and is constant perpendicular to this vector. A model disk, the transmission pattern, and the transmitted disk image are illustrated in Figure 2. This illustration is for an object at transit; at other times the fringe pattern is not aligned with north.

The key measurement from an LBTI observation is the ratio of the transmitted flux to the total photometric flux. Because the transmission pattern is designed to suppress light from the star, leaving light from a much fainter disk, this ratio is approximately the ratio of the transmitted disk flux to the stellar flux. Deriving the transmitted disk flux is not straightforward however, as some on-axis (i.e., stellar) flux is always transmitted because the instrument is not perfect and the star has a finite angular size. Removal of these effects is an integral part of the data analysis (see Defrère et al. 2015), so the quantity derived from a given observation is the "calibrated null depth" or "source null depth." In what follows, we generally refer to this measurement and the same quantity derived from our models as simply the "null depth." Because the total flux is almost exactly the stellar flux and dominates over any disk emission, we therefore compute the null depth for our models as the transmission for a starless model divided by the stellar flux density.

2.3.1. Disk Transmission Calculation

Our disk model is radially extended, but to illustrate how surface brightness is transmitted through the LBTI transmission pattern as a function of angular scale we first consider a series of discrete annuli of angular radii $\phi = r/d$. We later combine these annuli to model the transmission for our disk models.

The angular distance to the first transmission peak is $\phi_{null} = \lambda/(2B)$; for the LBTI $\lambda = 11\,\mu$m and $B = 14.4$ m, so the distance is 79 mas. The transmission function perpendicular to the fringes T_{null} is $\sin^2(\pi\phi/[2\phi_{null}])$, and is shown as the gray line in Figure 3, where the x axis is the distance from the annulus center in units of the distance to the first transmission peak (i.e., ϕ/ϕ_{null}). A common definition for the inner working angle of an instrument is where the sensitivity first reaches half of the peak value, which for LBTI is therefore at $\lambda/(4B) = 39$ mas.

To calculate the transmission for a point at some azimuth around the annulus requires finding the sky-plane component of this vector point (relative to the star) that is perpendicular to the fringe pattern. This component can be calculated using three rotations, and is

$$\phi_{proj} = \phi \times (\sin\Omega_{LBTI}\cos\theta + \cos\Omega_{LBTI}\sin\theta\cos i)\,, \quad (6)$$

where θ is the angle from the sky plane around the annulus to the point of interest, and Ω_{LBTI} is the position angle of the annulus relative to the LBTI fringe pattern. The angle Ω_{LBTI} varies with hour angle, and because the LBTI baseline is always perpendicular to the local vertical (i.e., a great circle through

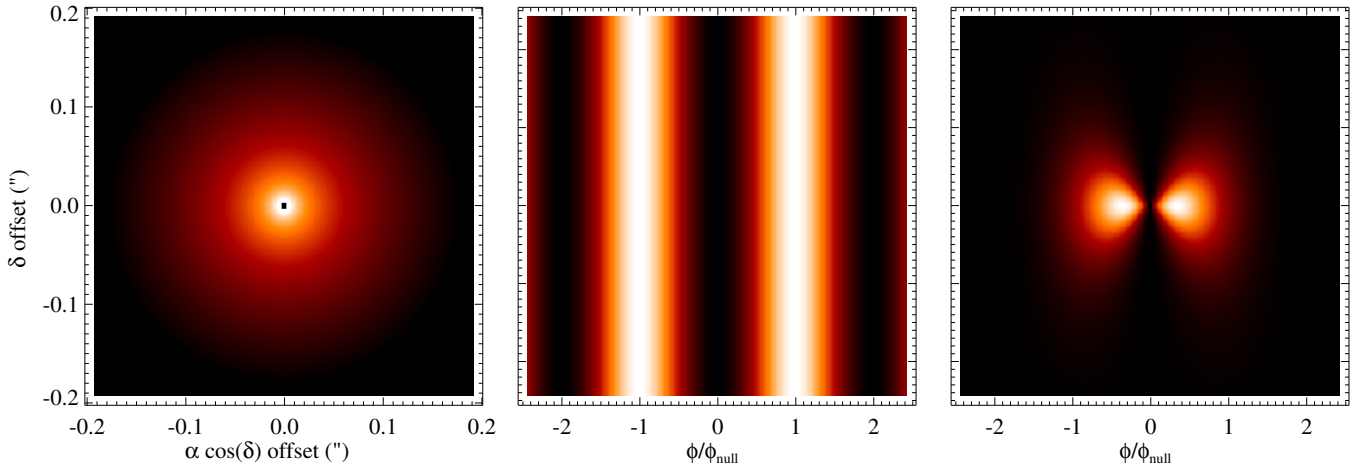

Figure 2. Illustration of LBTI transmission for a face-on disk observed at transit, where lighter regions correspond to greater disk surface brightness or greater LBTI transmission. All panels have the same spatial scale, but are labeled with different units (arcsec or $\phi_{\rm null}$). The left panel shows a face-on image of our disk model at 10 pc (the star has been omitted). The middle panel shows the LBTI transmission pattern projected on the sky, with bright fringes being transmission maxima. The convention for the angle $\Omega_{\rm LBTI}$ is also shown. The right panel shows the transmitted disk flux (i.e., the left panel multiplied by the middle panel). For real observations the LBTI detector sees the right panel convolved with the diffraction-limited beam of a single LBT mirror (with a FWHM of about 280 mas). The computed null depth is the total flux density in the right panel divided by the stellar flux density.

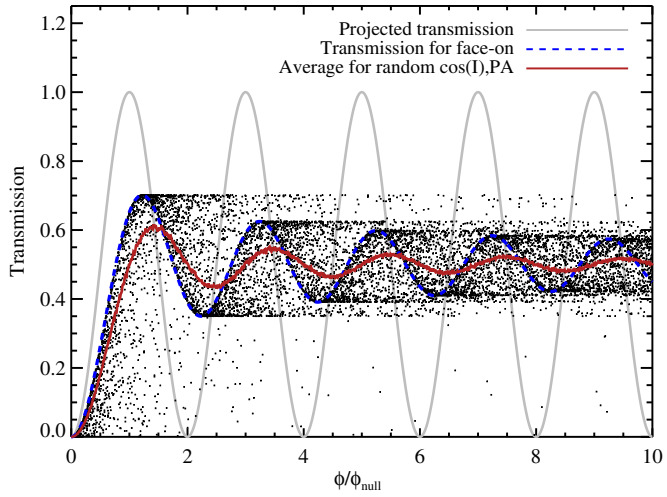

Figure 3. LBTI transmission for annuli of different angular sizes relative to the first transmission peak (where $\phi/\phi_{\rm null} = 1$). The gray line is the projected transmission function parallel to the LBTI baseline, the blue dashed line is the fraction of emission for face-on ($i = 0$) annuli after summing around the azimuthal angle. Dots show a population of annuli with random inclinations and position angles, and the red line shows the average transmission of these dots.

the target and zenith), is equal to Ω for an object at transit. The transmission from a point in the annulus is then[11]

$$T_{\rm null} = \sin^2(\pi\phi_{\rm proj}/[2\phi_{\rm null}])\,. \quad (8)$$

For a face-on ($i = 0$) annulus at radius ϕ, the transmission is clearly a function of azimuth around the annulus. Averaging around an annulus yields the total transmission for that annulus, and repeating this calculation for annuli of different angular sizes gives the blue dashed line in Figure 3.

[11] This transmission function is identical to the transmission at null given for the KIN by Millan-Gabet et al. (2011)

$$T_{\rm null} = (1 - \cos[2\pi\,(xu + yv)])/2, \quad (7)$$

where x, y are the sky offsets from the null center and u, v the corresponding spatial frequencies (i.e., $xu + yv = \phi_y B/\lambda$). LBTI transmission is simpler to compute because the length of the sky-projected baseline is always the same due to the common mount for the mirrors.

This exercise is finally repeated for a large number of annuli with random orientations, so that $\cos i$ is distributed evenly from 0 to 1, and $\Omega_{\rm LBTI}$ is evenly distributed from 0 to 180°. Again, the transmission around each annulus is azimuthally averaged, which results in the dots shown in Figure 3. Averaging these points yields the average transmission as a function of annulus radius for a population of disks with random orientations, shown as the red line. As can be surmised from the decreasing amplitude, the average transmission tends to 0.5 at large separations (i.e., the average of $\sin^2$ is 0.5). The minimum separation at which this transmission is achieved is $\phi_{\rm null}$, twice the inner working angle.

The origin of the dot distribution can be understood by considering how annuli of different orientations are transmitted through a given transmission peak. For example, the upper envelope of dots at about 70% transmission are all transmitted through the first transmission peak, and those at higher $\phi/\phi_{\rm null}$ are nearer to edge-on with position angles closer to $\Omega_{\rm LBTI} = 0°$ (i.e., perpendicular to the baseline and parallel to the fringes). This effect is relatively common because the average inclination is about 60° (i.e., biased toward edge-on). By comparing the phase of the gray line with the red line, it is clear that the peak average transmission is actually about a quarter of the way beyond a transmission peak, and that the peak transmission for face-on annuli lies somewhere in between. The phase shift of the face-on transmission can be understood by realizing that an annulus with a radius ϕ that is slightly greater than $\phi_{\rm null}$ has more emission in the peak transmission region than an annulus with $\phi = \phi_{\rm null}$. The average transmission for random orientations is phase shifted slightly further because most disks are inclined, and therefore on average appear somewhat smaller on the sky than they actually are.

2.4. Transmitted Disk Flux

Using the reference model of Section 2.2.2, Figure 4 shows the total and transmitted disk flux as a function of radius for a face-on geometry and a distance of 10 pc. That is, the figure is a histogram showing where the total and transmitted flux originates, so the solid line is an azimuthally summed radial profile created from the right panel of Figure 2. Much of the

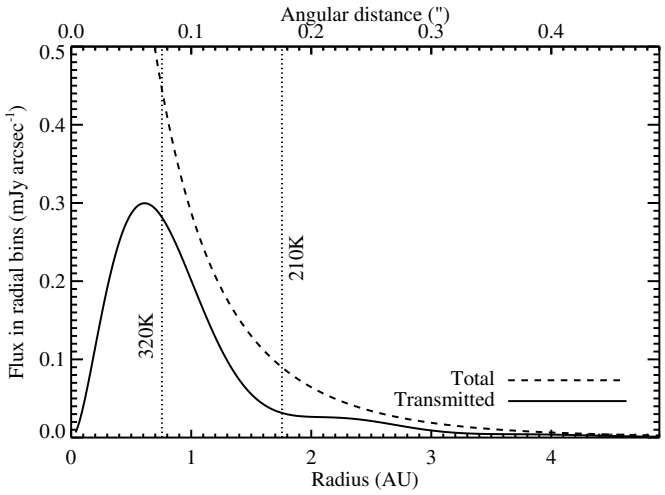

Figure 4. Total and transmitted flux density per unit radius, as a function of radius for a single face-on reference model disk at 10 pc. This plot therefore shows azimuthally summed radial profiles from the left and right panels of Figure 2. Flux is lost at all radii due to the transmission pattern, but most is lost from inside the habitable zone. The total and transmitted disk fluxes are 0.11 and 0.031 mJy.

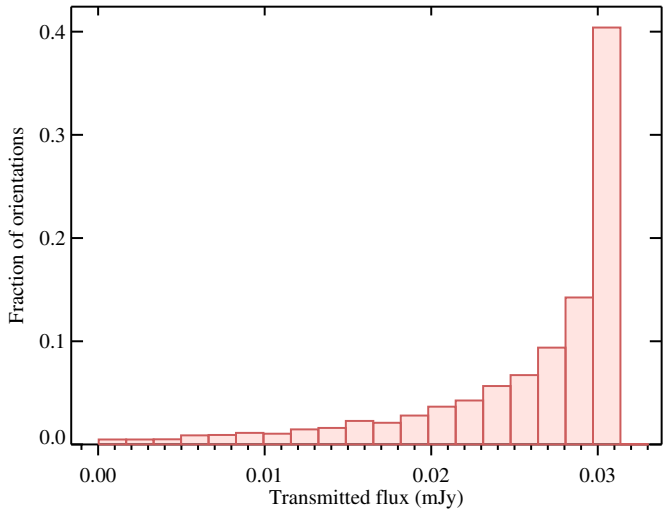

Figure 5. Distribution of transmitted fluxes for our reference model at 10 pc (with $z = 1$) and randomly distributed orientations. The dotted line shows the average transmitted flux derived in Figure 4. The disk will sometimes appear fainter than average, but is often a little bit brighter. The mean level is 0.026 mJy, and the medial level 0.029 mJy.

total disk emission originates from the inner regions, and since the disk inner edge is well inside the first transmission peak significant flux from these inner regions is not transmitted. Some flux is also lost at larger radii, and in total only about 30% of the disk flux is transmitted. Overall therefore, the radial distance over which the disk emits strongly in the mid-IR and can be detected is not particularly large; emission is strongly reduced inside the inner working angle, and the faint Wien side of cooler emission means that the surface brightness drops steeply at larger radii. Given the spacing of the transmission peaks and the distance to nearby stars, the transmitted flux detected by the LBTI is constrained to come from near the HZ, even if it cannot be certain that it originates within it.

Figure 5 shows how the total transmitted flux is distributed for a random distribution of disk orientations. The concentration of transmitted fluxes near the maximum arises because any disk with a position angle perpendicular to the transmission pattern has the same transmitted flux, regardless of inclination (and any disk near to face-on also has the same transmitted flux). The low transmitted flux tail arises from disks that have a position angle parallel to the transmission pattern and are sufficiently near to edge on such that almost the entire disk lies in the central null transmission region. Such a geometry is relatively unlikely, as can be seen by the lack of dots with low transmission in Figure 3. These relatively rare low transmitted fluxes are allowed because we assume disks with negligible scale height. This distribution therefore represents a pessimistic (but possible) case, and becomes tighter as the disk scale height increases. The width of the distribution also depends on the range of hour angles over which a target is observed, as discussed in Section 2.5.

The point here is that the transmitted flux depends on the orientation, and since this is expected to be unconstrained for LBTI targets (unless we use stellar inclination or the orientation of a resolved outer disk as an estimate, which will be possible for some of the HOSTS sample), there will be a corresponding uncertainty in any disk parameters that are derived from the observations.

Since the transmitted flux scales linearly with $\Sigma_{m,0}$, the distribution of $\Sigma_{m,0}$, and hence z, required to reproduce a given transmitted flux is directly related to that in Figure 5. The distribution of possible null depths for our reference model at 10 pc is therefore calculated by dividing the distribution of transmitted fluxes in Figure 5 by the stellar flux. The distribution of zodi levels z implied for a given observed null depth (or upper limit) is found by dividing the observed null depth by the distribution of model null depths for $z = 1$. This was the method employed by Millan-Gabet et al. (2011) in modeling KIN observations with `Zodipic`.

2.5. Sky Rotation

Any real LBTI observation takes a finite amount of time, during which any disk will rotate relative to the transmission pattern on the sky. Thus, even a vertically thin edge-on disk, which can be instantaneously invisible to the LBTI, will be visible when the length of the observation is taken into account.

To compute how the disk transmission changes for an observation of a given object requires computing the position angle of the LBTI fringe pattern on the sky at a given hour angle. The common mirror mount for the LBT means that this angle is the difference between the vector in the direction of the local vertical and a vector pointing toward equatorial north along a line of constant right ascension through the object in question (i.e., the hour circle). This angle is commonly called the parallactic angle.

The null depth is then computed as the average null depth over the range of observed hour angles. For modeling purposes here, these are spaced evenly in hour angle, but future models will use the true distribution for each specific observation. Figure 6 shows the difference between the instantaneous sensitivity for a transiting target (left panel) and a 4 hr observation (right panel), for a target at 60° declination over the parameter space of different disk orientations. This calculation is purely related to the changing position angle of the disk, and does not represent the time needed to reach a given S/N. Here, as before, we have assumed a vertically thin disk. The dark region in the upper middle of the left panel shows that an edge on disk is not instantaneously detectable when the disk is aligned with the LBTI fringe pattern. In the right panel, the rotation of the fringe

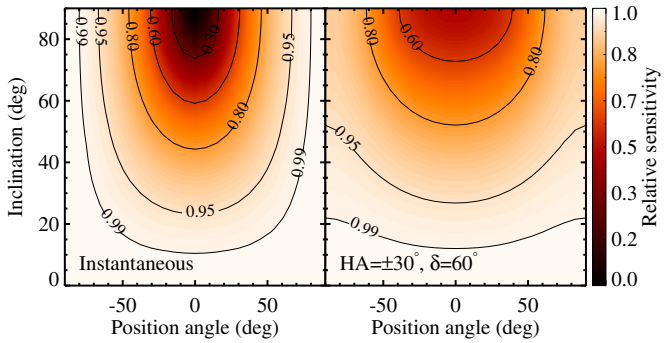

Figure 6. LBTI sensitivity relative to a face-on disk for instantaneous (left) and 4 hr (right) observations (the changing sensitivity is purely due to the changing position angle of the disk, not the time needed to reach a given S/N). An edge-on disk with $\Omega = 0^\circ$ is not instantaneously detected, but is only about 50% fainter than a face-on disk for a 4 hr observation.

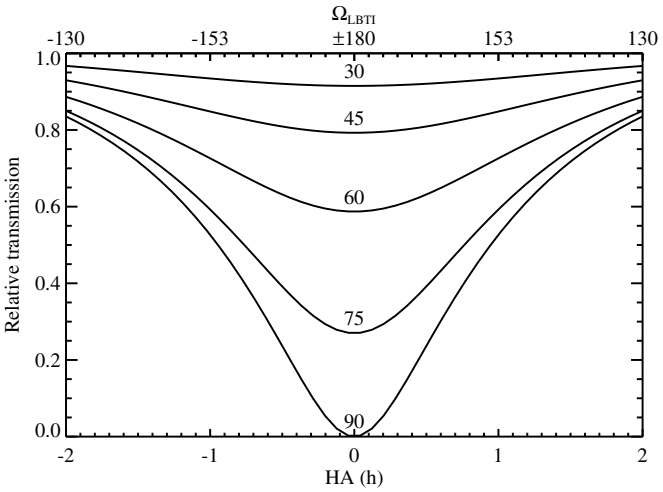

Figure 7. Instantaneous transmission through the LBTI over a range of hour angles for disks with $\Omega = 0^\circ$, relative to a face-on disk. Each line shows the transmission for a different disk inclination. The top axis shows the disk position angle relative to the fringe pattern, which is 180° at transit because the LBT is facing north at that time. The curves at transit (HA = 0) yield the transmission-inclination relation shown in the left panel of Figure 6 at $\Omega = 0$, while the average value of each curve yields the transmission-inclination relation shown in the right panel. The curve average is always greater than the transmission at transit, so observations over a wider range of hour angles can detect disks with less favorable orientations.

pattern with respect to north over a four hour observation means that the sensitivity relative to a face-on disk is reduced by about 50% for the worst case disk orientation.

To understand the origin of this increased sensitivity, Figure 7 again shows the transmission relative to a face-on disk, but now for $\Omega = 0$ at each point in the range of hour angles from −2 to 2 hr. Each curve shows how the transmission for a different disk inclination varies with hour angle (or $\Omega_{\rm LBTI}$). At HA=0, the curves correspond to a cut at $\Omega = 0$ in the left panel of Figure 6. The average of each line over the hour angle range corresponds to the same cut, but in the right panel. Because the average of each curve is greater than the minimum value at HA=0, the disk sensitivity is greater.

Of course, the inclination and position angle dependence in Figures 6 and 7 shows that it would be highly desirable to discern how the transmitted disk flux changes as a function of hour angle in order to learn about the disk geometry and the possibility of non-axisymmetric structure. For axisymmetric disks there is also a potential degeneracy between the disk geometry and the vertical scale height; an edge-on disk with sufficient vertical extent will vary much less than the curves in Figure 7, and may be indistinguishable from a less inclined disk that is oriented such that the transmission variation is small. If a large variation in transmission is seen, the disk may be vertically thin, but could alternatively be non-axisymmetric. The detection of such effects will certainly be sought, but given that we expect most LBTI detections to be near the sensitivity limits and therefore at low S/N we assume for now that LBTI observations can be modeled by simply averaging over the hour angle.

2.6. Linking LBTI to Other Observations

The LBTI is well suited to observing dust levels in the habitable regions around nearby stars, both in terms of baseline length and observing wavelength. LBTI results will therefore broadly address the goal of characterizing warm dust levels without requiring additional information from other observations. However, the specific location and radial extent of the dust will be poorly constrained, and as illustrated by Figure 4, significant disk emission can arise from regions both inside and outside the habitable zone and still be detected with the LBTI. In general, such degeneracy in disk models will be hard to break because the goal of the LBTI is to detect disks that are fainter than current detection limits (hence the need for the modeling framework outlined in this paper).

In some cases, however, LBTI results will be compared to other observations, most likely (spectro)photometric detections or limits for the total disk flux density at the same wavelength, and in some cases limits on disk size from high-resolution imaging or interferometry. Detections and/or upper limits from near-IR interferometry will provide constraints on dust levels inside the LBTI IWA. LBTI will similarly provide very strong constraints on the emission spectrum and location of hot dust detections (Absil et al. 2013; Ertel et al. 2014).[12] Mid-IR photometric data will come from *Spitzer* InfraRed Spectrograph (IRS; Werner et al. 2004; Houck et al. 2004), WISE observations (Wright et al. 2010), or in the future the spectrometers on the Mid-Infrared Instrument (MIRI) on the *JWST*, which cover the same wavelength range as the LBTI. Such photometry will provide the most useful constraints on the disk location, so we now briefly outline how the total and LBTI-transmitted disk fluxes vary with model parameters, in particular the disk inner and outer radii.

To illustrate the flux density distribution, Figure 8 shows disk spectra for our reference model with $z = 1$, with examples for both Sun-like and A-type host stars at 10 pc. Because our standard model has the same temperature range all disk spectra have the same shape, but are brighter or fainter depending on the zodi level, the distance to the host star, and the host star spectral type (which changes the area of the disk and hence total brightness). The A5V star has $L_\star = 14\,L_\odot$, so the disk around this star is 14 times brighter than for the Sun-like star. However, the A-star is only about 5 times brighter at 11 μm (10 vs. 2 Jy), so the disk/star flux ratio has increased by a factor of about 3.

Figure 8 also shows how the spectrum varies when $r_{\rm in}$, $r_{\rm out}$, and α are changed from their standard values, and what the effect is at the LBTI wavelength of 11 μm. Larger values of α concentrate the disk emission closer to the star, and hence

[12] Unless the dust has a very high albedo ($\gtrsim$0.9), non-detection with high quality mid-IR photometry is already sufficient to restrict this dust to lie well inside the habitable zone (Kennedy et al. 2015).

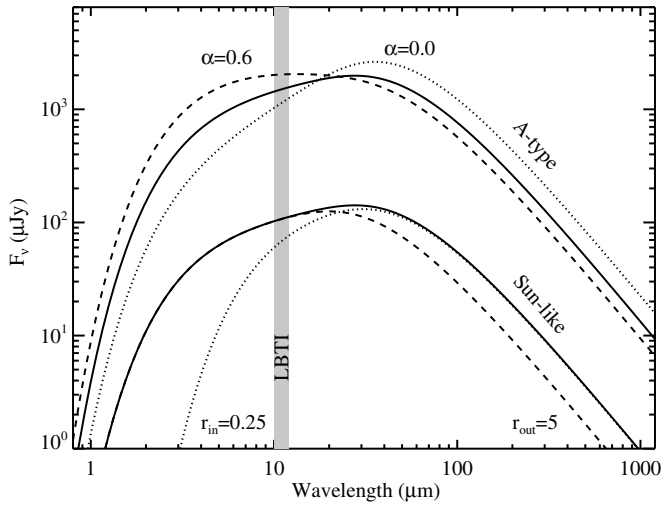

Figure 8. Change in the disk spectrum with model parameters. The solid lines show the reference model for a Sun-like star (lower) and an A-type star (upper), both at 10 pc. All disks have the same spectrum shape regardless of spectral type, but at fixed distance the total brightness increases to earlier spectral types that have physically larger disks. The dotted and dashed lines show how the spectrum changes for different values of r_{in} and r_{out}, or for two different values of α (the defaults are $r_{in} = 0.034$ AU, $r_{out} = 10$ AU, $\alpha = 0.34$). The LBTI N' band is shown as a gray stripe.

shift the spectrum toward warmer temperatures. Changing r_{in} and r_{out} remove emission from the inner and outer disk regions, leading to a spectrum that is closer to a single-temperature black body spectrum. As noted above and shown by the curve for $r_{out} = 5$ AU, the outer disk radius is large enough that the exact value matters little for the level of emission at 11 μm.

While our model gives a reasonable idea of the true disk spectrum, and could in principle be used to constrain disk structure based on observations at other wavelengths, it is inaccurate on a detailed level because grains do not emit like black bodies. Three important differences are that (1) the disk will be fainter than our model at long wavelengths because grains emit inefficiently at wavelengths longer than their size, (2) the spectrum may also be shifted to shorter wavelengths due to the presence of small grains with temperatures greater than that of a black body, and (3) the spectrum may show non-continuum spectral features. These differences pose problems for extrapolating our model to other wavelengths, or at least mean that additional parameters such as grain properties would need to be considered.

Such differences are of minor importance here, however, as important comparisons with other observations can be made at the LBTI wavelength, so are largely independent of the disk spectrum. The most important comparison is between the total and transmitted disk fluxes, or equally the total disk to star flux ratio and the null depth. To illustrate why combining such measurements is important, Figure 9 shows how the total and transmitted model disk flux changes at 11 μm as the disk inner and outer radii change. As r_{in} is increased the total disk flux decreases because hot emission is being removed. However, the LBTI-transmitted flux changes little while r_{in} remains small, because these changes occur behind the central transmission minimum and are invisible. When r_{in} is outside the first transmission peak (at about 0.7 AU here) both the total and transmitted fluxes decrease in the same way. As r_{out} is decreased there is initially little difference in the total and transmitted fluxes because the outer disk is faint at 11 μm, but when r_{out} moves behind the central transmission minimum the flux drops much more steeply than the total flux. As noted earlier, Figure 9 shows that the LBTI transmission is insensitive to our choice of disk inner and outer radii, as long as the disk is much wider than the habitable zone.

Given such relations between the total and transmitted disk fluxes, it is clear that observations of both may constrain the disk location. However, the transmitted disk flux is a function of both the disk size and the orientation, so the best constraints on the disk size require the orientation to be known (or take some assumed value). It is unlikely that the position angle will be inferred from LBTI measurements in many cases, so the disk orientation would probably be assumed based on other system information, such as coplanarity with a resolved outer cool disk component, the known inclination and/or position angle of the host star's rotation axis (Le Bouquin et al. 2009; Greaves et al. 2014), or of planet orbits (Reidemeister et al.

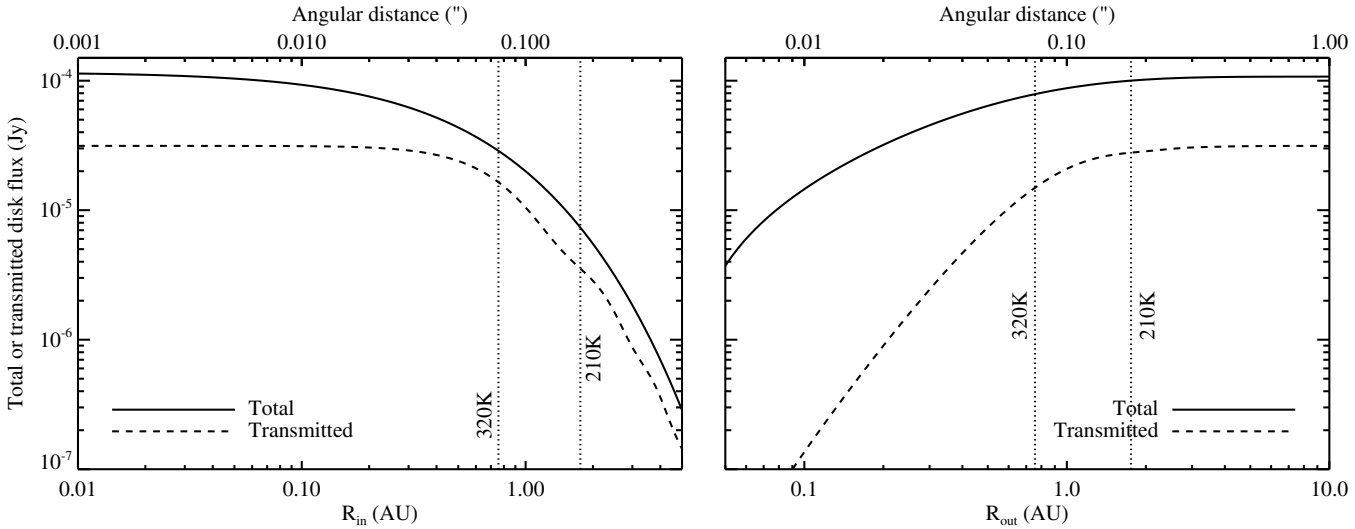

Figure 9. Change in total disk flux (solid lines) and transmitted disk flux (dashed lines) at 11μm as a function of r_{in} (left) and r_{out} (right), for a face-on reference model disk around a solar-type star at 10 pc. The total disk flux decreases as r_{in} increases, but is less sensitive to decreasing r_{out} because most of the mid-IR disk emission comes from the inner part of the disk (see also Figure 8). The transmitted flux is insensitive to the disk extent when r_{in} lies inside the first transmission peak and r_{out} lies outside the first transmission peak (i.e., at about 0.7 AU at 10 pc).

2009), or a combination of all three (Kennedy et al. 2013). See Defrère et al. (2015) for an application of this assumption to η Crv.

2.7. Scattered Light Surface Brightness

Currently, NASA is focused on developing concepts for three optical (0.4–1 μm) exoplanet-imaging missions, Exo-C (a coronagraph), Exo-S (a starshade), as well as an ambitious precursor, the coronagraph on WFIRST-AFTA. Therefore, the thermal dust emission information from the LBTI must be converted to predict the impact on scattered light imaging. We now derive a simple prescription for converting the dust levels in the above model into scattered light surface brightness estimates.

Scattered light predictions are in general difficult, and have largely proven unsuccessful to date (e.g., Krist et al. 2010), with debris disks imaged in scattered light generally seen to be much fainter than predicted based on theoretical grain models that match observed thermal emission. The typical minimum grain size in debris disks is thought to 1–10 μm for Sun-like stars (e.g., Gustafson 1994; Krivov 2010; Pawellek et al. 2014), and the steepness of the size distribution means that these grains dominate the surface area. Such grains are expected to scatter optical light fairly isotropically, and have fairly large albedos of $\gtrsim$0.5. The scattered light faintness of debris disks, where albedos of 0.05–0.1 are seen (e.g., Kalas et al. 2005; Golimowski et al. 2011; Meyer et al. 2007), likely arise from incorrect assumptions about grain properties and sizes, and how these grains scatter starlight.

The properties of exo-zodi are not sufficiently well known that considering physically motivated possibilities for different grain sizes and properties would make predictions for their scattered light brightness more certain. Therefore, regardless of the physical reason, we will assume that the ~0.1 effective albedos seen for scattered light disks around nearby stars are representative, and assume isotropic scattering. It may be that the properties of warm dust are different to those inferred from scattered light detections, since for example hot dust detected with near-IR interferometry is generally inferred to originate in much smaller grains (e.g., Defrère et al. 2011; Lebreton et al. 2013). For higher/lower albedos, our scattered light predictions would be higher/lower by the same factor.

While the model surface density $\Sigma_{\rm m}$ is connected to the true optical depth and the surface area of grains from which the emission arises, the model surface density is the true optical depth only if the grains behave like black bodies. That is, real grains reflect starlight, so the true total surface area in the disk is always higher than $\Sigma_{\rm m}$. To be more realistic, and to allow for the possibility of scattered light, the grain absorption and scattering properties need to be considered.

Consider a disk with particles with a range of sizes D, and $\Sigma_{\rm true}(D)dD$ the true cross-sectional area per unit area of particles in the size range D to $D+dD$. Using the absorption efficiency as a function of size and wavelength $Q_{\rm abs}(\lambda, D)$, the thermal emission is

$$S_{\rm th} = 2.35 \times 10^{-11} \int \Sigma_{\rm true}(D) Q_{\rm abs}(\lambda, D) B_\nu(\lambda, T[D]) dD. \quad (9)$$

Though the dependence is not included explicitly here for simplicity, all quantities in this equation also vary with location in the disk due for example to the disk structure and changing composition. Using the scattering efficiency $Q_{\rm sca}(\lambda, D)$ the scattered light emission can be written in various ways, but a convenient form is

$$S_{\rm sca} = \frac{F_{\nu,\star}}{4\pi} \left(\frac{d}{r}\right)^2 \int \Sigma_{\rm true}(D) Q_{\rm sca}(\lambda, D)\, dD, \quad (10)$$

which we could also express in terms of albedo $\omega = Q_{\rm sca}/(Q_{\rm abs}+Q_{\rm sca})$ by substituting $Q_{\rm sca} = Q_{\rm abs}\omega/(1-\omega)$. If we assume the albedo ω is the empirical value of 0.1, independent of grain size and wavelength, then because $Q_{\rm abs} = 1-\omega$ the surface density $\Sigma_{\rm m}$ is approximately the true optical depth, but is underestimated by a factor of $1-\omega$ (i.e., $\Sigma_{\rm m} = \Sigma_{\rm true}[1-\omega]$). That is, with these assumptions the thermal surface brightness could be written

$$S_{\rm th} = 2.35 \times 10^{-11} \Sigma_{\rm true} B_\nu(\lambda, T_{\rm BB})(1-\omega). \quad (11)$$

The scattered light brightness is therefore calculated using the dust surface density and the empirical effective albedo. With these assumptions, the predicted scattered light emission from the model of Section 2.2 would be

$$S_{\rm sca} = \frac{F_{\nu,\star}}{4\pi} \left(\frac{d}{r}\right)^2 \frac{\omega}{1-\omega} \Sigma_{\rm m}. \quad (12)$$

For simplicity we use the value of $\Sigma_{\rm m}$ derived from our modeling, and thus include an extra factor of $1/(1-\omega)$. Therefore, with our model the scattered light surface brightness relative to the stellar flux[13] in the habitable zone (i.e., $r = r_0$) of a 1 zodi disk decreases as $1/L_\star$, as the habitable zone is pushed farther from the star by the increased luminosity. This is the approach we use below to estimate the limiting scattered light surface brightnesses for HOSTS, and for the LBTI η Crv detection.

An extension to this approach would be to add a phase function that accounts for forward scattering properly. The albedo could then be derived theoretically and calibrated with observations. While in the above case the scattered light can be calculated simply along the radial direction, and for a given orientation turned into an image, use of a phase function $g(\theta)$ requires a three-dimensional calculation that includes the star-particle-observer scattering angle θ at each location in the disk. Given that we expect relatively large uncertainties in disk parameters, even in the case of a detection, use of a detailed three-dimensional calculation including (assumed) grain properties and a phase function will in general be unwarranted.

To convert the simple scattered light prediction of Equation (12) to an observable for an arbitrary disk inclination, a three-dimensional calculation must be made to account for brighter disk ansae. However, the disk inclination will in general be unknown, so a simple approximation for deriving a representative scattered light surface brightness would be to assume an average inclination of $4/\pi$, and for a vertically thin disk an increase of $1/\cos(4/\pi) \approx 3$.

3. MODELING LBTI OBSERVATIONS

We now show two examples using the model described above. We first use the LBTI commissioning measurement for η Crv to illustrate how zodi levels are derived, and then derive zodi limits for the HOSTS survey. These levels assume that the disk orientation is not known, but in some cases coplanarity with a resolved outer disk could be assumed to further constrain the

[13] The dust surface brightness relative to the stellar flux is the relevant quantity here, because the light scattered from a putative exo-Earth will scale with the stellar flux in the same way as the dust.

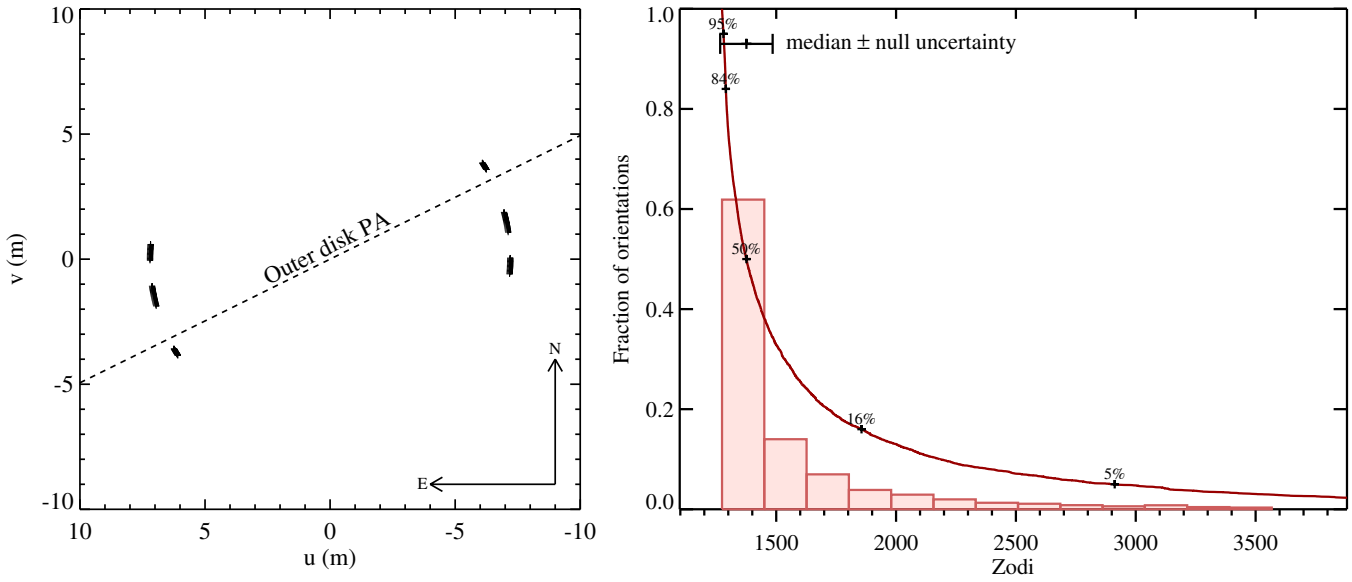

Figure 10. LBTI observation and zodi distribution for η Crv. The left panel shows the uv coverage and outer disk position angle. The right panel shows the distribution of zodi levels for 5000 random disk orientations. The cumulative distribution of zodi levels is shown by the gray line. The median zodi level and the uncertainty purely due to the null depth uncertainty is also shown.

disk brightness. This assumption can be made for η Crv, and we refer the reader to Defrère et al. (2015) for an in-depth discussion of these results for this system.

3.1. Generic Zodi Level Calculation

Using η Crv with a null depth of 4.4% ± 0.35% as an example, we first show how the distribution of zodi levels is derived assuming an unknown disk orientation. This procedure is generic in that it can be applied to any LBTI observation, whether a significant detection or an upper limit was found. The LBTI is still in commissioning so the zodi sensitivity derived here is not illustrative of the expected performance.

Figure 10 shows the uv plane coverage of the LBTI observation relative to the disk position angle, and the distribution of zodi levels calculated using our reference model. We include the rotation of the disk relative to the fringe pattern during the observation to compute the average null depth for each disk orientation. As described at the end of Section 2.4, the distribution is essentially the inverse of that shown in Figure 5.

The distribution is strongly peaked at about $z = 1350$, with a tail of larger values due to unfavorable disk orientations. The 1σ zodi uncertainty due purely to the calibrated null depth measurement is given by the width of the "median ± null uncertainty" error bar in the right panel of Figure 10. Similarly, the 16% and 84% levels from the cumulative distribution give a representative 1σ range due to the orientation distribution. The upper uncertainty on the zodi level is therefore set by the orientation distribution, while the lower uncertainty is set by the null depth measurement. The median zodi level for η Crv is $z = 1376 \pm 102$ if the uncertainty is set by the LBTI null depth measurement. Including the 1σ range from the orientation distribution in quadrature, the range covered on either side of the median value is $1236 < z < 1869$. In general, we expect that the null depth uncertainty will dominate the lower bound on the zodi level, and the orientation distribution will dominate the upper bound.

For comparison, based on a KIN detection and using the `Zodipic` model Mennesson et al. (2014) found $z = 1813 \pm 209$ for η Crv at 8.5 μm with no assumptions about the disk orientation. Our derived zodi level is different for two reasons: (1) η Crv is hotter than the Sun (6900 K), so our luminosity-dependent zodi definition will lead to a zodi level about 1.7 times smaller than `Zodipic`, and (2) the mid-IR spectrum of the η Crv disk increases more steeply with wavelength than a black body (i.e., has a silicate spectral feature), so although our model has nearly the same temperature profile as `Zodipic`, our derived zodi level will be slightly larger because LBTI observes at 11 μm. Therefore, direct comparisons between our zodi levels and those using `Zodipic` should not be made.

3.1.1. Generic Scattered Light Surface Brightness

Using the simple prescription for the scattered light surface brightness described in Section 2.7, we can convert the zodi levels shown in Figure 10 into a prediction for the face-on scattered light surface brightness. Here, the value of interest is the surface brightness in the habitable zone, as this is where planets would be sought. The level is then calculated using Equation (12), with $\Sigma_{\rm m} = z\Sigma_{\rm m,0}$ because $\Sigma_{\rm m,0}$ is the value at the radial distance where the equilibrium temperature is the same as Earth's. Adopting $\omega = 0.1$, and using $F_{\nu,\star} = 72.35$ Jy in the V band, $d = 18.3$ pc, $r = \sqrt{L_\star/L_\odot} = 2.3$ AU, and $z = 1372^{+497}_{-140}$ yields a scattered light surface brightness of $S_{\rm sca} = 4.0^{+1.4}_{-0.4}$ mJy arcsec^{-2}, or about 15 mag arcsec^{-2}. As noted above, this habitable zone estimate may be increased by a factor of a few to account for the inclination of the disk.

3.2. Exo-zodi Detection Limits for HOSTS

Given a prediction for the sensitivity of the LBTI and a sample of stars that will be observed, we can make predictions for the sensitivity of the HOSTS survey. In what follows we assume a 1σ uncertainty on the LBTI calibrated null depth of 10^{-4}, and hence the limits presented are also at 1σ. Limits are calculated as above, using the median of the distribution of zodi levels over the random distribution of orientations. Though we do not account for it here, there is some uncertainty in the stellar flux densities and luminosities used, which we estimate to contribute

at about the 5% level. Here we calculate the sensitivity assuming an observation at a single hour angle, but when the model is applied to real observations in the future the calculations will account for sky rotation as described in Section 2.5.

These calculations are carried out for both our reference disk model, and a "worst-case" scenario where the dust is restricted to lie only within the habitable zone, which we assume to lie between temperatures of 320 and 210 K. As shown in Figures 4 and 9, the LBTI is sensitive to emission that lies interior and exterior to the habitable zone, so the dust surface density must be higher in the latter case for an LBTI detection at the same sensitivity. As noted above in Section 2.2.3, the "zodi levels" derived with this different radial structure are also different and should really be considered as enhancements over the surface density derived for the solar zodiacal cloud, rather than zodi levels to be compared with other values.

The HOSTS survey sample is described by Weinberger et al. (2015), the key aspect being that targets are chosen such that their habitable zones have larger angular sizes than the first LBTI transmission peak, so observations directly probe the levels of habitable zone dust. The sample is split by $B-V$ color at 0.42 into "Sun-like" and "sensitivity" sub-samples, which simply reflects the levels of dust that can be detected.

Figure 11 shows the predicted disk to star flux ratios, null depths, and sensitivity in zodi units for the HOSTS sample using our reference model (red and blue symbols) and our worst case scenario (gray symbols, which we discuss below). The top and middle panels show the flux ratios and null depths expected for a 1 zodi model around these stars, and the bottom panel shows the sensitivity in zodis for the predicted LBTI sensitivity. There are clear trends with stellar luminosity, which can be understood as follows. With our model the disk flux density at fixed wavelength scales with the angular area, i.e., $\propto z\Sigma_{\rm m,0}L_\star/d^2$ (with our zodi definition $\Sigma_{\rm m,0}$ is constant, but we include it to consider other zodi definitions below). The stellar flux, on the other hand, scales $\propto L_\star/(T_\star^3 d^2)$ in the Rayleigh–Jeans regime so the total disk to star flux ratio only depends on the star, and is higher for earlier spectral types

$$\frac{F_{\rm disk}}{F_{\nu,\star}} \propto z\Sigma_{\rm m,0}T_\star^3\,. \tag{13}$$

This dependence in the top panel of Figure 11 arises due to the stronger scaling of stellar luminosity with temperature than flux density at 11 μm, with the variations from a perfect correlation arising due to variation in $L_\star$ at fixed $T_\star$ (i.e., different stellar radii). At fixed distance, as the stellar temperature and luminosity increase the habitable zone is pushed outward ($\propto\sqrt{L_\star}$) and its area and brightness increase more rapidly than the stellar flux. Alternatively, for a fixed disk angular size (and hence fixed disk brightness), increasing the stellar temperature and luminosity pushes the system to greater distances and the star becomes fainter due to increasing distance faster than it becomes brighter due to an increased temperature.

The null depths for a 1 zodi disk are shown in the middle panel, and the trend has a similar origin as the disk to star flux ratio. At fixed distance, increasing stellar luminosity increases the disk surface brightness at fixed angular radius because r_0 increases (i.e., increases if α is positive). Assuming that most of the transmitted disk flux originates from a constant angular scale (i.e., near the first transmission peak), the transmitted disk flux therefore increases as $\propto(\sqrt{L_\star}/d)^\alpha$ (assuming that the effect of the changing disk temperature in the first transmission peak is small). Combining this expression with the stellar flux yields a

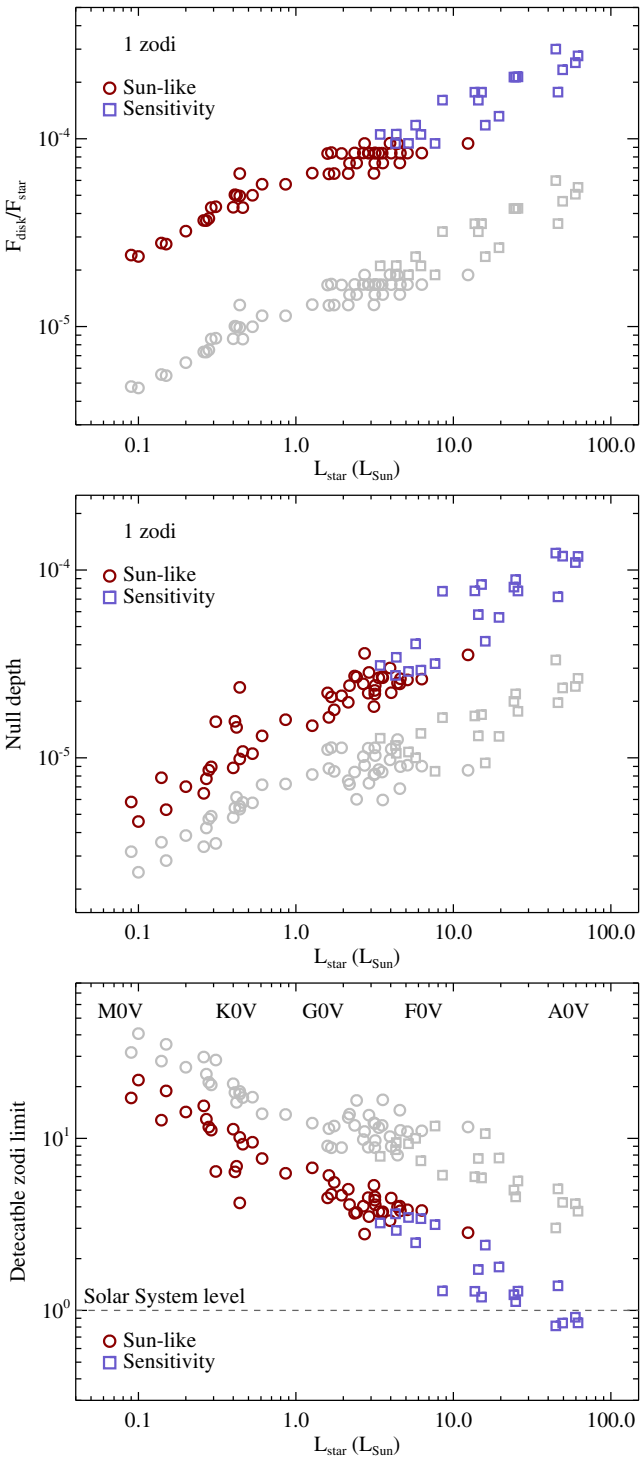

Figure 11. Disk to star flux ratio, null depth, and zodi limits for the reference disk model for HOSTS survey stars, split into "Sun-like" and "sensitivity" sub-samples (red circles and blue squares). The top two panels show the flux ratio and null depth for a 1 zodi disk, and the bottom panel shows the sensitivity in zodis for the predicted LBTI sensitivity. The dashed line in the bottom panel shows the solar system level. Gray symbols show a pessimistic narrow-disk scenario where disks only cover the habitable zone (from 320 to 210 K), and the different disk width means that these values are not strictly zodi levels because they do not use our reference model (see Section 2.2.3).

null depth

$$\text{null} \propto z\Sigma_{\rm m,0}T_\star^3\left[\left(\sqrt{L_\star}/d\right)^\alpha\right]. \tag{14}$$

HOSTS stars are chosen to have habitable zones with similar angular sizes and for our reference model $\alpha = 0.34$, so the term

in square parentheses varies relatively little and the null depth almost entirely depends on the stellar temperature.

The absolute null depth level of course also varies linearly with the zodi level, so the zodi limits can be derived by dividing the expected sensitivity of 10^{-4} by the null depth values in the middle panel (i.e., by solving Equation (14) for z)

$$z \propto \Sigma_{\rm m,0}^{-1} T_\star^{-3} \left[\left(d/\sqrt{L_\star} \right)^\alpha \right]. \quad (15)$$

The resulting sensitivities show that what we define as solar system levels of zodiacal dust are at the predicted 1σ noise level for early-type stars, as are 3–10 zodi disks around Sun-like stars.

This discussion of scalings applies equally to the narrow worst case scenario, shown as gray symbols in Figure 11. As expected for a narrower disk that emits over a smaller total physical area, the disk to star flux ratios are lower than for our reference model, as are the null depths. While the difference between the two models is about a factor of five in disk/star flux ratio, the difference in null depths is only a factor of two to three because most of the flux removed from the disk in the narrower model is hidden behind the central transmission minimum (e.g., Figure 9). Similarly, the difference in zodi levels is a factor two to three higher in this case compared to our reference model. Therefore, the effect of this pessimistic scenario in terms of habitable zone dust levels is relatively minor.

Because our zodi definition is based on constant surface density in the habitable zone, the z dependence on luminosity directly shows that the LBTI can truly detect lower surface densities of dust in the habitable zones of earlier type stars. This conclusion does not depend on our zodi definition because the LBTI is sensitive to $\Sigma_{\rm m}(r_0)$. A different definition, for example $z \propto F_{\rm disk}/F_\star$, makes the zodi limit approximately constant ($\propto [d/\sqrt{L_\star}]^\alpha$), but also implies $\Sigma_{\rm m,0} \propto T_\star^{-3}$ (and the sensitivity to habitable zone surface density is the same as with our definition).

3.2.1. Scattered Light for HOSTS

Given the detection limits in the bottom panel of Figure 11, we can also derive the face-on habitable zone ($r = r_0 = \sqrt{L_\star/L_\odot}$ AU) scattered light surface brightness of disks at the HOSTS survey detection limits. These limits are shown in Figure 12 for $\omega = 0.1$ as defined in Section 2.7. Red and blue symbols show limits for our standard disk model, which again depend on the stellar luminosity.

The origin of the dependence on stellar luminosity can be understood by rewriting Equation (12) using the zodi limit scaling above

$$S_{\rm sca} \propto \frac{F_{\nu,\star}}{T_\star^3} \left(\frac{d}{\sqrt{L_\star}} \right)^{2+\alpha}. \quad (16)$$

Like the zodi limits, the scattered light levels in the habitable zone at these limits decrease with stellar luminosity. The squared distance and luminosity dependence is simply the geometric effect that accounts for $1/r^2$ dilution of light and that surface brightness is an angular measure. The extra α dependence is because the habitable zone is not at the first transmission peak for all targets. If the LBTI observation is dominated by emission near the first transmission peak, but the habitable zone is slightly farther out (i.e., $d/1{\rm pc}/\sqrt{L_\star/L_\odot} > 1$), the α dependence represents a model-dependent extrapolation that is relatively unimportant while α is small.

As with the LBTI sensitivity to habitable zone surface density, our zodi definition has no effect on the scattered light predictions

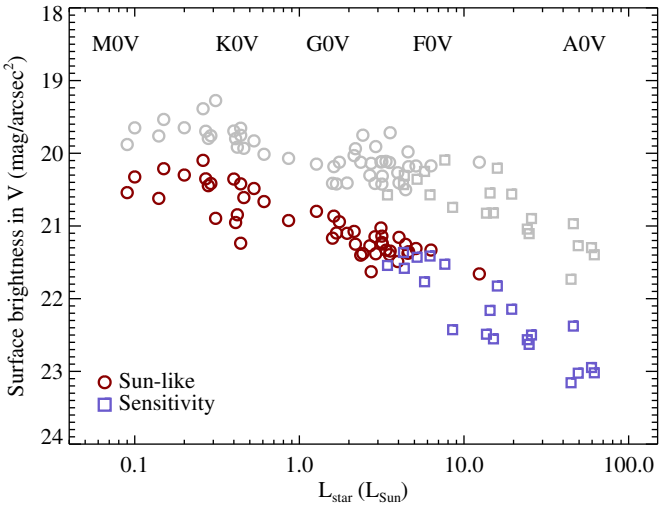

Figure 12. Face-on V-band habitable zone scattered light surface brightness limits (assuming $\omega = 0.1$) for the reference disk model for HOSTS survey stars, split into "Sun-like" and "sensitivity" sub-samples (red circles and blue squares). These limits use Equation (12) and the zodi limits from Figure 11. Gray symbols show a pessimistic narrow-disk scenario where disks only cover the habitable zone (from 320 to 210 K).

and is merely an intermediate step for deriving the true quantity of interest. That is, as described above the LBTI sensitivity to $\Sigma_{\rm m}$ in the habitable zone (i.e., $z\Sigma_{\rm m,0}$), which sets the limits on $S_{\rm sca}$, will always be the same. For the example of a constant $F_{\rm disk}/F_\star$ zodi definition therefore, z is constant but $\Sigma_{\rm m,0} \propto T_\star^{-3}$ and Equation (16) is the same.

Because the HOSTS sample is explicitly chosen such that the LBTI is sensitive to thermal emission from dust in the region of interest for Earth-imaging, the scattered light predictions do not strongly depend on the choice of our disk model parameters (but of course depends on albedo). The predictions are not totally independent of our disk model however, since for example changing the steepness of the radial profile makes the dust in the model more or less concentrated relative to the LBTI transmission pattern, thus changing the derived zodi level. Varying α between -1 and 1 yields changes of $\lesssim$1 mag in the scattered light predictions, meaning that the model dependent uncertainty is similar to the variation expected from the unknown disk inclination.

For solar-type stars, the scattered light levels in Figure 12 for our face-on reference model at the ~4 zodi detection limit is 20–21 mag arcsec^{-2}. For comparison, using a 4 zodi disk the `Zodipic` model predicts 21.2 mag arcsec^{-2} at 1 AU with default parameters (a solar analog with $\omega = 0.18$ and use of a phase function), and 21.6 mag arcsec^{-2} for $\omega = 0.1$ and isotropic scattering. Our simple model therefore compares well with the more complex calculation made by `Zodipic`. For a 60° inclined disk, `Zodipic` gives 21.1 mag arcsec^{-2}, and for 90° gives 20.6 mag arcsec^{-2}, and therefore the increase from face-on to edge-on is about 1 magnitude. Our model has smaller vertical extent than `Zodipic`, so the increase in surface brightness for inclined disks will be larger, roughly a factor of three for a 60° inclined disk.

The gray symbols in Figure 12 show the scattered light surface brightness for narrower disks that only lie in the habitable zone. These limits are about one magnitude brighter than our reference model, so similar to the variation in brightness with the (unknown) disk orientation. Therefore, the scattered light limits from LBTI observations are fairly robust to disk width.

4. SUMMARY AND CONCLUSIONS

We have outlined a parameterized disk model to be used for modeling and interpreting mid-IR exo-zodi observations with the LBTI. Using this model, we have illustrated how to derive dust limits and levels for exo-zodiacal clouds, and how these can be converted to scattered light surface brightnesses needed for planning future missions that will image extrasolar Earth-analogs.

Using the HOSTS sample that the LBTI will observe, we illustrate the survey detection limits both in terms of zodi units and the expected scattered light levels at these limits. These limits are around ten times the solar system level for solar-type stars, and thus the LBTI is expected to provide stringent limits with key information that will help plan future Earth-imaging efforts.

The Large Binocular Telescope Interferometer is funded by the National Aeronautics and Space Administration as part of its Exoplanet Exploration Program. This work was supported by the European Union through ERC grant No. 279973 (G.M.K., O.P., A.B.S., and M.C.W.). We thank the reviewer for valuable comments. Part of this work was performed at the Jet Propulsion Laboratory, California Institute of Technology, and at the NASA Exoplanet Science Center (NExScI), under contract with NASA.

REFERENCES

Absil, O., Defrère, D., Coudé du Foresto, V., et al. 2013, A&A, 555, A104
Absil, O., Eiroa, C., Augereau, J., et al. 2010, in ASP Conf. Ser. 430, Pathways Towards Habitable Planets, ed. V. Coudé Du Foresto, D. M. Gelino, & I. Ribas (San Francisco, CA: ASP), 293
Bracewell, R. N. 1978, Natur, 274, 780
Brown, R. A. 2014, ArXiv:1402.2612
Defrère, D., Absil, O., Augereau, J.-C., et al. 2011, A&A, 534, A5
Defrère, D., Hinz, P. M., Skemer, A. J., et al. 2015, ApJ, 799, 42
Ertel, S., Absil, O., Defrere, D., et al. 2014, A&A, 570, 128
Golimowski, D. A., Krist, J. E., Stapelfeldt, K. R., et al. 2011, AJ, 142, 30
Greaves, J. S., Kennedy, G. M., Thureau, N., et al. 2014, MNRAS, 438, L31
Gustafson, B. A. S. 1994, AREPS, 22, 553
Houck, J. R., Roellig, T. L., van Cleve, J., et al. 2004, ApJS, 154, 18
Jackson, A. P., & Wyatt, M. C., MNRAS, 425, 657
Kalas, P., Graham, J. R., & Clampin, M. 2005, Natur, 435, 1067
Kasting, J. F., Whitmire, D. P., & Reynolds, R. T. 1993, Icar, 101, 108
Kelsall, T., Weiland, J. L., Franz, B. A., et al. 1998, ApJ, 508, 44
Kennedy, G. M., & Wyatt, M. C. 2013, MNRAS, 433, 2334
Kennedy, G. M., Wyatt, M. C., Bryden, G., Wittenmyer, R., & Sibthorpe, B. 2013, MNRAS, 436, 898
Kopparapu, R. k., Ramirez, R., Kasting, J. F., Eymet, V., et al. 2013, ApJ, 765, 131
Krist, J. E., Stapelfeldt, K. R., Bryden, G., et al. 2010, AJ, 140, 1051
Krivov, A. V. 2010, RAA, 10, 383
Le Bouquin, J.-B., Absil, O., Benisty, M., et al. 2009, A&A, 498, L41
Lebreton, J., van Lieshout, R., Augereau, J.-C., et al. 2013, A&A, 555, A146
Mennesson, B., Millan-Gabet, R., & Serabyn, E. 2014, ApJ, 797, 119
Meyer, M. R., Backman, D. E., Weinberger, A. J., & Wyatt, M. C. 2007, in Protostars and Planets V, ed. B. Reipurth, D. Jewitt, & K. Keil (Tucson, AZ: Univ. Arizona Press), 573
Millan-Gabet, R., Serabyn, E., Mennesson, B., et al. 2011, ApJ, 734, 67
Nesvorný, D., Jenniskens, P., Levison, H. F., et al. 2010, ApJ, 713, 816
Pawellek, N., Krivov, A. V., Marshall, J. P., et al. 2014, ApJ, 792, 65
Reidemeister, M., Krivov, A. V., Schmidt, T. O. B., et al. 2009, A&A, 503, 247
Roberge, A., Chen, C. H., Millan-Gabet, R., et al. 2012, PASP, 124, 799
Serabyn, E., Mennesson, B., Colavita, M. M., Koresko, C., & Kuchner, M. J. 2012, ApJ, 748, 55
Stark, C. C., Roberge, A., Mandell, A., & Robinson, T. D. 2014, ApJ, 795, 122
Werner, M. W., Roellig, T. L., Low, F. J., et al. 2004, ApJS, 154, 1
Weinberger, A. J., Bryden, G., Kennedy, G. M., et al. 2015, ApJS, 216, 24
Wright, E. L., Eisenhardt, P. R. M., Mainzer, A. K., et al. 2010, AJ, 140, 1868
Wyatt, M. C., Smith, R., Greaves, J. S., et al. 2007, ApJ, 658, 569